Structural characterization of the interaction of α-synuclein nascent chains with the ribosomal surface and trigger factor

Annika Deckert[a,b], Christopher A. Waudby[a,b], Tomasz Wlodarski[a,b], Anne S. Wentink[a,b], Xiaolin Wang[a,b], John P. Kirkpatrick[a,b], Jack F. S. Paton[a,b], Carlo Camilloni[c], Predrag Kukic[c], Christopher M. Dobson[c], Michele Vendruscolo[c], Lisa D. Cabrita[a,b,1], and John Christodoulou[a,b,1]

[a]Institute of Structural and Molecular Biology, University College London, London WC1E 6BT, United Kingdom; [b]Institute of Structural and Molecular Biology, Birkbeck College, University of London, London WC1E 7HX, United Kingdom; and [c]Department of Chemistry, University of Cambridge, Cambridge CB2 1EW, United Kingdom

The ribosome is increasingly becoming recognized as a key hub for integrating quality control processes associated with protein biosynthesis and cotranslational folding (CTF). The molecular mechanisms by which these processes take place, however, remain largely unknown, in particular in the case of intrinsically disordered proteins (IDPs). To address this question, we studied at a residue-specific level the structure and dynamics of ribosome-nascent chain complexes (RNCs) of α-synuclein (αSyn), an IDP associated with Parkinson's disease (PD). Using solution-state nuclear magnetic resonance (NMR) spectroscopy and coarse-grained molecular dynamics (MD) simulations, we find that, although the nascent chain (NC) has a highly disordered conformation, its N-terminal region shows resonance broadening consistent with interactions involving specific regions of the ribosome surface. We also investigated the effects of the ribosome-associated molecular chaperone trigger factor (TF) on αSyn structure and dynamics using resonance broadening to define a footprint of the TF–RNC interactions. We have used these data to construct structural models that suggest specific ways by which emerging NCs can interact with the biosynthesis and quality control machinery.

NMR spectroscopy | ribosome | nascent chain | α-synuclein | cotranslational folding

Within living systems, protein biosynthesis takes place at the peptidyl transferase center (PTC) of the ribosome, where peptide bond formation occurs at a rate of ~20 amino acids per s (1) to generate a nascent chain (NC) that subsequently emerges through the exit tunnel (2), an ~100-Å passage that can accommodate *ca*. 30 residues (3). On emerging from the tunnel, NCs can begin to explore their conformational landscapes, where about a third of cytosolic proteins in *Escherichia coli* are expected to acquire native-like structure cotranslationally (4, 5). Cotranslational folding (CTF) may, therefore, be a key process to assist NCs in adopting their native folds by minimizing the exposure of hydrophobic regions and reducing the risk of misfolding and aggregation (6, 7).

To ensure the production of correctly folded and functionally active proteins, further mechanisms have evolved to regulate folding pathways. Evidence indicates that the ribosome itself can modulate the folding process (8) by reducing the rate of tertiary contact formation and inhibit misfolding by stabilizing unfolded states (9). Fluorescence depolarization measurements have also shown that the dynamics of emerging NCs can be constrained (10), particularly those with a positive charge (11), owing to interactions with the negatively charged ribosome surface, which are said to create a protective environment within the crowded cell (12).

CTF processes within the cell can also be modulated by chaperones (13). In *E. coli*, the first chaperone encountered by an emerging NC is trigger factor (TF), which binds transiently to the ribosome via a docking site on protein L23 (14, 15), forming a cradle above the exit tunnel. It has been proposed that TF promotes CTF in several ways, including by shielding exposed hydrophobic stretches (16),

inhibiting premature folding (17), and by unfolding preexisting structures and intermediate states (8). TF binds to nontranslating ribosomes with a K_d of *ca*. 1 μM (18), but this affinity can be significantly stronger in the presence of NCs [depending on their sequences (19) and lengths (20)]. TF comprises three distinct structural regions: an N-terminal ribosome-binding domain, a peptidyl-prolyl isomerase domain (PPD), and a centrally located, C-terminal substrate-binding domain (SBD). An NMR study of the interactions of free TF with the isolated, unfolded protein PhoA (21) identified four binding sites within TF, of which three are located within the SBD and one in the PPD. The regions of PhoA that interacted most strongly with these sites were found to be rich in hydrophobic and aromatic residues, in accord with the known substrate preferences of TF (19).

Although structural studies of CTF are still few, solution-state nuclear magnetic resonance (NMR) of translationally arrested NCs is emerging as a powerful means of reporting high-resolution details (22–25), despite the high molecular weight (2.5 MDa) of ribosome-nascent chain complexes (RNCs) (26), with their low working concentrations (~10 μM) and limited lifetimes. Furthermore, computational approaches based on molecular dynamics (MD) simulations have also been developed to investigate the nature and properties of CTF (27, 28) processes, although the large size of the ribosome and relatively slow rates of protein synthesis and folding still pose major challenges for all-atom

---

Significance

Protein biosynthesis is carried out by ribosomes, the macromolecular machines present in all kingdoms of life. Aided by molecular chaperones, nascent proteins can begin to fold while emerging from the ribosome. Achieving their native fold, and avoiding misfolding, is thereby crucial for the fate of all newly synthesized proteins. The molecular details of this fundamental process, however, are poorly understood. In this work we develop a combined NMR and molecular simulation approach to characterize the behavior during biosynthesis of α-synuclein (αSyn), an intrinsically disordered protein associated with Parkinson's disease. The detailed interactions of αSyn with the ribosome surface and with trigger factor, a ribosome-associated chaperone, reveal the first steps of how a nascent chain emerges from the ribosome.

calculations on appropriate time scales. To circumvent this problem, coarse-grained methods have been adopted to allow the inherent properties of a system to be preserved while using a reduced molecular representation to minimize the number of elements in the simulations (29).

Here we show that combined NMR and MD studies of RNCs of α-synuclein (αSyn), a protein whose aggregation is associated with Parkinson's disease (PD), can provide insight into the conformations sampled by a disordered polypeptide chain during synthesis, complementing information emerging from studies of the CTF of globular proteins, as well as existing structural descriptions of αSyn that have been obtained for the protein in isolation (30) and within cells (31, 32).

Results

αSyn Is Disordered on the Ribosome. αSyn RNCs, translationally arrested using the SecM motif (33), were generated in *E. coli* (Fig. 1A), and the samples were purified based on our previous method (34), with the removal of the N-terminal His(H_6)-tag using tobacco etch virus (TEV) protease (Fig. S1 A and B). The ^{1}H-^{15}N selective optimized flip-angle short transient heteronuclear multiple quantum coherence (SOFAST-HMQC) (35) spectra with nonuniform weighted sampling sensitivity enhancement (36) were acquired (Fig. 1B) alongside biochemical analyses (37) (Fig. 1F and Fig. S1 C–F) and ^{15}N-heteronuclear stimulated echo (XSTE) diffusion measurements (38) (Fig. S1 G–I) to monitor the integrity of the RNC, which showed that the NC was attached and that the samples remained essentially completely stable for ~72h.

The ^{1}H-^{15}N NMR correlation spectrum of the αSyn RNC (Fig. 1B) shows a narrow range (8.0–8.8 ppm) of amide proton chemical shifts (CS) characteristic of an intrinsically disordered protein (IDP) and overlays closely with a matching spectrum of isolated αSyn (Fig. S2B) in the presence of an equimolar concentration of 70S (Fig. 1 C and D). CS differences were uniformly small ($\Delta\delta_{NH}$ < 0.05ppm, Fig. S3A), indicating that the NC samples a range of disordered state conformations similar to isolated αSyn, which allowed the transfer of cross-peak assignments to that of the RNC (Fig. 1B). Owing to line broadening and overlap in the RNC spectrum, 63 αSyn resonances, from M5-D135, were resolved sufficiently to enable their intensities to be analyzed. Critically, the observation of the D135 resonance (Fig. 1 B and E), located just 28 residues from the PTC, indicates that the NC possesses extensive mobility near the opening of the exit tunnel.

Resonance Broadening Indicates Interactions of αSyn with the Ribosome Surface. In contrast to the minimal CS perturbations observed in the NC, large reductions in the intensities of NC resonances were observed relative to those of isolated αSyn (Fig. 1 D and E). This effect provides a sensitive probe of the changes in NC dynamics associated with the gain in mobility of the polypeptide chain as it emerges from the exit tunnel, and with the loss of mobility arising from interactions with the ribosome surface.

The intensities of cross-peaks in the RNC spectrum were reduced by >87% relative to isolated αSyn in the presence of ribosomes, with substantial variation across the sequence (Fig. 1E). The C-terminal resonances were highly broadened, but from residue D135–K58 resonances were generally observed to become narrower (and hence more intense), indicating that the NC mobility is increased as residues become more distant from the exit tunnel. However, from K58 to the N terminus this trend is reversed as resonances are progressively broadened, resulting in decreased intensities. These results indicate an increasing propensity of this region to interact with the ribosome surface, which seems to be correlated with a high density of positively charged residues. In contrast, the negatively charged C-terminal region remains observable, despite its increased proximity to the ribosome surface. In addition to these long-range trends, two clusters of residues, M5–S9 and V37–V40, were broadened beyond detection, whereas intensities in a third region centered around T92/G93 were attenuated to a lesser extent. These clusters seem to be associated with the aromatic residues F4, Y39, and F94, rather than generally
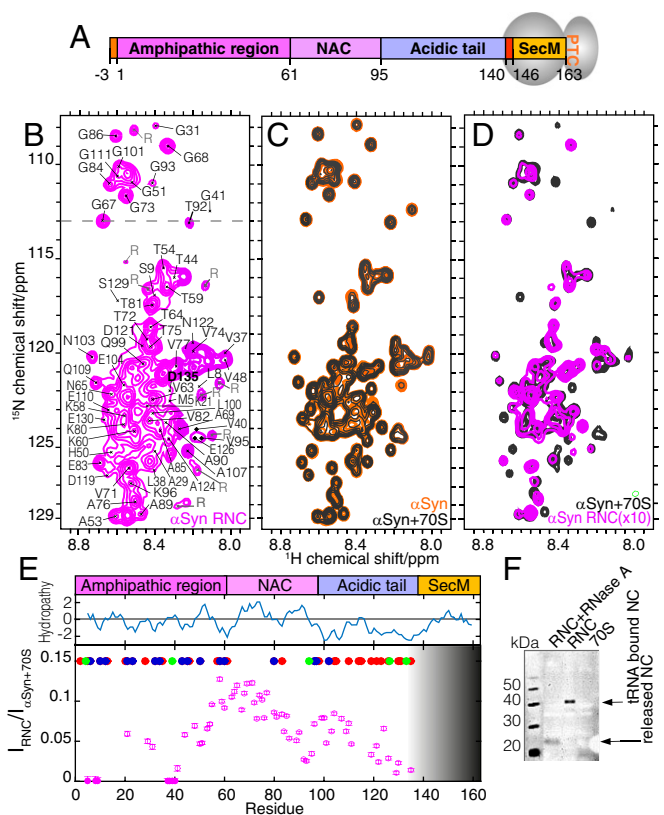

Fig. 1. NMR characterization of the αSyn RNC. (*A*) Schematic of the αSyn RNC construct. (*B*) The ^{1}H-^{15}N SOFAST-HMQC spectrum of the αSyn RNC and resonance assignments; R indicates 70S background peaks. (*C*) Comparison of ^{1}H-^{15}N SOFAST-HMQC spectra of isolated αSyn with and without 1 mol eq of ribosomes. (*D*) Comparison of the αSyn RNC spectrum in *B* with αSyn in the presence of 70S in *C*; RNC intensities amplified. (*E*) Cross-peak intensities in the αSyn RNC relative to isolated αSyn in the presence of ribosomes; the gray-shaded area depicts the approximate length of the exit tunnel. A Kyte and Doolittle hydropathy plot and an amino acid classification of the αSyn protein sequence in positively charged (blue), negatively charged (red), and aromatic (green) residues is also shown. (*F*) Anti-SecM Western blot to probe for RNC integrity, showing tRNA-bound (~40 kDa) and released αSyn NCs (~20 kDa).

with hydrophobicity because the most hydrophobic region of the sequence, N65–T75, is also the region of greatest intensity.

For comparison, we also examined changes in the intensity of isolated αSyn in the presence of ribosomes. Reductions in intensity of up to 60–70% were observed for N-terminal residues (M5, L8, and S9), without any perturbations to the C-terminal region (Fig. S2C). This broadening of N-terminal resonances is comparable to that observed in the αSyn RNC, suggesting that similar interactions occur with the ribosomal surface in both cases, although the effect is substantially weaker in the absence of the covalent tethering in the RNC. Further analyses of charged isolated αSyn variants suggested that the polypeptide–70S interactions are at least in part due to electrostatic interactions (Fig. S4).

To probe the dynamics of the NC in more detail, ^{1}H linewidths were measured in spectra of the RNC and isolated αSyn (Fig. 2A and Fig. S3B). RNC resonances were found to have significantly broader linewidths (and hence larger R_2 relaxation rates) than those in isolated αSyn, with an increase in R_2 from 37 ± 7 s^{-1} (mean $\pm$ SD) for the isolated protein to 109 ± 38 s^{-1} in the RNC (Fig. 2B). To determine the significance of such values, we estimated the R_2 values that might be expected for a NC immobilized by tight binding to the ribosome surface. The ^{1}H-^{1}H dipolar interactions were calculated using an ensemble model of the αSyn RNC (discussed in *Structural modeling of the αSyn*
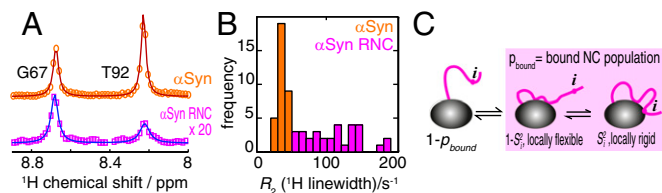
Fig. 2. The ^{1}H linewidth analysis of the αSyn RNC. (*A*) The ^{1}H cross-sections through ^{1}H-^{15}N SOFAST-HMQC spectra (δ_N113.15 ppm, Fig. 1*B*, dashed line) of isolated αSyn and the αSyn RNC fitted to a sum of Lorentzian functions (solid lines) to determine ^{1}H R_2 rates. (*B*) Distribution of R_2 values obtained from lineshape fitting of residues selected from V48–A124 for isolated αSyn (34 residues) and the αSyn RNC (31 residues). (*C*) Schematic depicting the exchange of the NC between its free and ribosome-associated states. The globally bound state consists of a population-weighted average of a locally flexible state, where residue *i* is highly dynamic but in close proximity to residues tethered nearby, and a locally rigid state with residue *i* being in direct contact with the ribosome surface. The relative proportions of these states are described by the generalized order parameter, S^2.

RNC), taking the rotational correlation time of the ribosome to be 3.9 μs at 277 K (39), from which we estimate the amide proton relaxation rates of the bound state to be $16.1 \pm 4.4 \times 10^3$ s^{-1} (Fig. S3*C*). Using this estimate, and making the assumption that NC resonances are in fast exchange between free and ribosome-associated states, as is typically the case for weak interactions, the observed relaxation rates will be a population-weighted average of the free and bound states (24). Thus, using the observed linewidths of residues between V48 and A124 (Fig. 2*B*), the estimated population of this NC segment bound to the ribosome surface is $0.45 \pm 0.24\%$ (Fig. S3*D*). Although this number could be increased if the bound state were to be significantly mobile (Fig. 2*C*), this analysis nevertheless indicates that these interactions are of a weak and transient nature. It is likely that interactions with the ribosome surface for other segments of the NC, whose resonances are more severely broadened and so cannot be observed (Fig. 1*E*), could be considerably stronger.

NMR Analysis of TF–NC Interactions. To examine the impact of a ribosome-associated chaperone on the behavior of the αSyn NC, [^{2}H,^{13}CH$_3$-ILV]-labeled TF was titrated into a ^{15}N-labeled sample of the αSyn RNC. Although ribosome-bound αSyn has been shown to be a weak substrate for TF (40, 41), TF itself has a moderate affinity for nontranslating 70S ribosomes [K_d ~1 μM (18)]. This combination of affinities was important in allowing saturation of the NC–TF interaction without the complication of strong NC binding causing substantial line broadening. We found that the addition of 1 mol eq of TF induced only small amide CS perturbations ($\Delta\delta_{NH} < 0.06$ ppm; Fig. 3*A* and Fig. S5*A*), indicating that the NC samples a similar distribution of disordered conformations as it does in the absence of TF. We observed, however, large and nonuniform reductions in the intensities of the αSyn cross-peaks (Fig. 3*B*), which enabled the nature of the TF–NC interaction to be analyzed. The intensities of residues K21–G111 in the RNC spectrum were reduced to $30 \pm 8\%$ of those observed in the absence of TF, whereas resonances of residues D119–D135 in the C-terminal region were less strongly perturbed, with relative intensities reduced only to $88 \pm 12\%$ (Fig. 3*B*). No effects on the resonances of residues N-terminal to K21 could be determined, because these resonances are already broadened beyond detection in the absence of TF (Fig. 1*E*). The addition of TF concentrations higher than 1 mol eq caused no further intensity changes in the RNC spectrum, indicating that, although the TF–NC interaction may be weak, the TF–70S interaction itself had reached saturation (Fig. 3*C*).

Analysis of the ^{1}H,^{13}C spectrum of TF showed that methyl resonances experienced large reductions in intensity in the presence of ribosomes (approximately sixfold relative to isolated TF; Fig. S5*D*), but little additional broadening was observed in the presence of the

αSyn NC (Fig. 3*D*), which is consistent with previous observations using fluorescence techniques that showed no increased recruitment of TF to ribosomes carrying an αSyn NC (41). For comparison, we examined changes in the spectrum of isolated αSyn in the presence of 1 mol eq of TF. At concentrations of 5 μM only small intensity changes (<5%) were observed, in residues located at the N terminus of αSyn. However, additional line broadening was evident at higher concentrations (100 μM), or in the presence of ribosomes (which promote the dissociation of the TF dimer) (Fig. S5*C*). Thus, although αSyn is indeed a weak TF substrate there is nevertheless some propensity to interact, and this may be promoted by the ribosome and, particularly, by the colocalization of TF and the NC during translation.

Structural Modeling of the αSyn RNC. Coarse-grained simulations of the αSyn RNC were used to develop a model with which to explore the structure and dynamics of the NC and to investigate potential sources of the NMR resonance broadenings observed. Here, we used the CamTube force field (42), in which the polypeptide chain is represented as a flexible tube as a means of describing its overall architecture. This approach increases the efficiency of sampling protein conformations relative to all-atom simulations, making it particularly effective for the study of large and flexible systems such as RNCs. Starting structures for the simulations were constructed from cryo-EM models of SecM-stalled translating ribosomes, where the 17-residue arrest sequence has an extended conformation in the exit tunnel (43), and structural ensembles for the NC were then generated from a 2.4-μs trajectory (Fig. 4*A* and Movie S1). From this ensemble, we found that the first NC residue to be located in the exit vestibule was D135, 28 residues (78 Å) from the PTC. Critically, this point coincides with the experimental observation of NC resonances, and the subsequent increase in intensity from D135 toward the N terminus (Fig. 1*E*). To estimate the rotational mobility of each residue within the NC, the structural ensemble was used to calculate S^2 order parameters, where a value of 1 describes rigid residues and a value of 0 describes fully flexible residues. We found that the observed increase in NMR intensities from D135–E104 (Fig. 1*E*) was associated with a decrease by two orders of magnitude in the calculated amide S^2 values (Fig. 4*C*), as well as a large increase in mobility as described by the Cα root mean square fluctuations (RMSF) (Fig. 4*D*). However, both parameters also
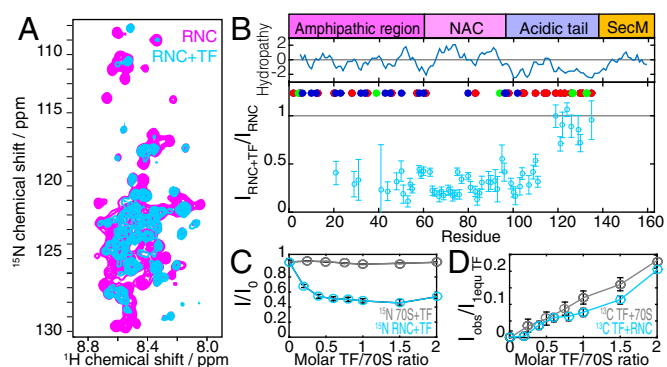
Fig. 3. NMR analysis of the interaction of TF with αSyn RNCs. (*A*) Comparison of ^{1}H-^{15}N SOFAST-HMQC spectra of the αSyn RNC with and without 1 mol eq TF. (*B*) Relative cross-peak intensities of the αSyn RNC following addition of TF. A Kyte and Doolittle hydropathy plot and an amino acid classification of the αSyn protein sequence in positively charged (blue), negatively charged (red), and aromatic (green) residues is shown. (*C*) Changes in the integrals of ^{15}N-edited ^{1}H amide envelopes of the αSyn RNC and ^{15}N-labeled 70S ribosomes with increasing TF. (*D*) Changes in the integrals of ^{13}C-edited ^{1}H methyl envelopes with increasing TF, in the presence of αSyn RNC (6.5 μM 70S) and 70S ribosomes (5 μM 70S). Integrals have been normalized to a 10 μM sample of isolated TF scaled according to the 70S concentration (neglecting effects of the TF monomer/dimer equilibrium).

predict a continued gain in mobility for residues more distant from the PTC, whereas the NMR data showed reduced peak intensities for residues in the vicinity of T92/G93 and for the N-terminal region (M5–V40) (Fig. 1E). We thus conclude that the observed perturbations in NMR peak intensity are the likely consequence of a combination of electrostatic effects induced by positively charged residues in the N terminus and interactions with aromatic residues (F4/Y39/F94).

The simulations were repeated in the presence of ribosome-bound TF, using a starting structure based on an NMR model of TF in complex with the disordered state of PhoA (21) (Fig. 4B and Movie S2). We observed that the αSyn residues K21–G111, which experienced the strongest reduction in resonance intensities on TF binding (~70%) (Fig. 3B), were able to contact proposed substrate binding sites in TF previously identified in the absence of the ribosome (21). Conversely, we found that the C-terminal residues D119–D135, which were only marginally broadened (~12%) upon TF binding, were not able to contact sites within TF. Interestingly, reductions in Cα RMSF values and S^2 order parameters were observed in the presence of TF for residues between E126 and the N terminus (Fig. 4 C and D). However, no TF-induced perturbations in NMR signal intensities were observed experimentally in the vicinity of E126 (Fig. 3B), suggesting that TF interactions do not occur within this region. Thus, whereas our modeling suggests that a restriction in mobility could be experienced from residues from E126, the NMR data show that interactions of the NC and TF seem only to occur from residues G111, presumably when these can begin to reach and interact with the TF cradle (Fig. 4B).

Using the simulated RNC structures we identified ribosomal proteins accessible to the NC and also mapped the changes in NC accessibility of the ribosome surface that occur upon TF binding. Fig. 4E illustrates the accessibility of the ribosome surface for the NC, which was calculated as the distance of closest approach between the backbone atoms of the NC and atoms of the 70S surface. Regions close to the exit tunnel, which are within 10 Å of the NC (in red), include the ribosomal proteins L17, L22, and L32, which are important binding sites for protein biogenesis factors (44) such as peptide deformylase and methionine aminopeptidase, as well as L23, L24, L29, L32, and rRNA. Upon binding of TF, the NC formed additional contacts with the chaperone at the expense of other regions of the ribosome surface, which became sterically occluded (Fig. 4F). Fig. 4G indicates the changes of the NC surface accessibility in the presence and absence of TF (compare Fig. 4 E and F). Regions corresponding to the ribosomal proteins L3, L17, L19, L22, and L32 (blue) became inaccessible upon binding of TF but as a consequence other regions (in red), including L4 and L28 as well as parts of L9 and L24, were sampled more often by the NC (Fig. 4H).

Discussion

We have used high-resolution solution NMR and coarse-grained MD to characterize the structure, dynamics, and interactions of αSyn NCs during biosynthesis on the ribosome. The limited solubility of RNC samples together with the observed NMR line broadening resulted in very weak signal intensities, equivalent to just 50–100 nM concentrations of isolated αSyn. Nevertheless, a combination of methodological advances, including longitudinal relaxation optimized experiments and nonuniform weighted sampling (35, 36), have enabled quantitative measurements to be made of CSs and cross-peak intensities for the majority of NC residues. Most importantly, a combination of biochemical and noninvasive spectroscopic assays were applied to ensure that all NMR signals analyzed in this study arise from intact, ribosome-bound NCs (Fig. 1F and Fig. S1 D and F–I).

Previous RNC structural studies have focused almost exclusively on examining folding competent globular proteins such as FLN5 (22, 25), SH3 (24) domains, and barnase (23). In contrast to folded states, which correspond to deep minima in free energy landscapes, IDPs have relatively flat free energy landscapes (45) that are highly sensitive to external perturbations [e.g., from
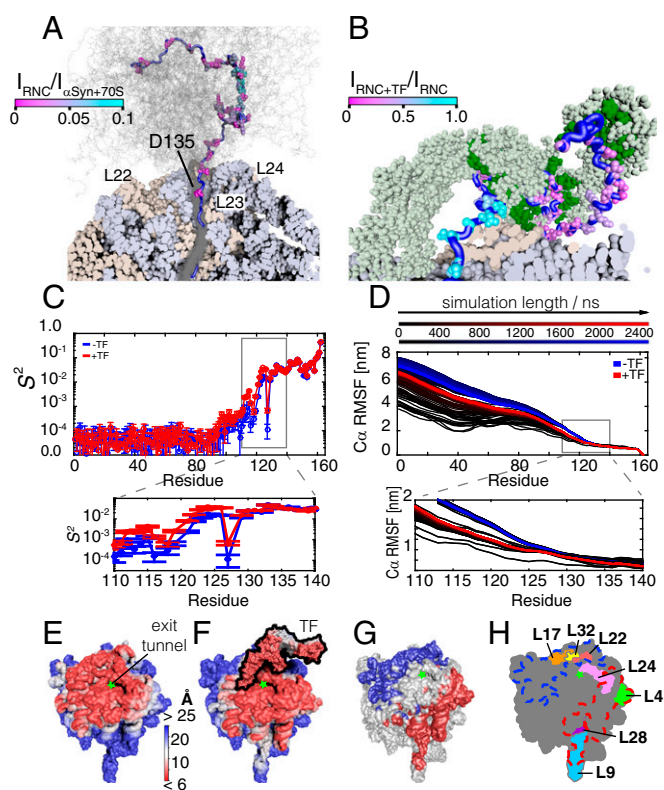

Fig. 4. Structural modeling of the αSyn RNC. (A) Cross-section of the simulated αSyn RNC showing the NC ensemble (gray) with a representative NC structure highlighted (blue), ribosomal proteins (beige), and RNA (blue-gray). Observed NMR resonances (relative to isolated αSyn in the presence of 70S , Fig. 1E) are shown as spheres colored according to their relative intensity (Fig. 1E). (B) αSyn RNC model with TF monomer (light green) and substrate binding pockets (21) (dark green); the observed NC resonances are shown as spheres colored according to the relative intensity in Fig. 3B. For clarity, residues 1–31 are not shown. (C) Amide S^2 order parameters determined from simulated ensembles with and without TF. (D) Cα RMSF of the αSyn RNC calculated over increasing lengths of the simulation trajectory, with and without TF. (E) Ribosome surface colored according to the distance of closest approach of the simulated NCs and (F) ribosome and TF surfaces colored as described in E. (G) Difference in ribosome surface accessibility (distance of closest approach) on TF binding. Blue regions become sterically restricted, whereas red regions represent parts of the ribosome surface that are more frequently contacted by the NC due to the steric restrictions imposed by TF on other parts of the ribosome surface. (H) Schematic diagram of ribosomal proteins in close proximity to the exit tunnel; ribosome orientation as in E–G.

mutations (46), posttranslational modifications (47), or from the intracellular environment (48)]. The investigation of IDPs therefore allows a detailed exploration of the accessible conformational space for a polypeptide chain, without complications of folding.

NMR CSs are typically sensitive probes of protein structure, yet we found that αSyn amide CS perturbations resulting from ribosomal attachment, or from the presence of TF, were extremely small (Figs. S3A and S5 A and B). By contrast, the intensities of cross-peaks in spectra of the RNC were highly variable relative to isolated αSyn (Fig. 1 D and E). The tethered motion of the NC inevitably affects NMR linewidths, given the thousand-fold difference in the effective rotational correlation times of the ribosome and of isolated αSyn. Residues will therefore generally gain independent mobility as they become more distant from the PTC and emerge from the exit tunnel. In this study, the residue closest in sequence to the PTC to be NMR-detectable was D135, from which point resonance intensities increased to a maximum at K58 (Fig. 1E). Our structural modeling indicated that the position of D135, 28 residues from the PTC, coincides with the emergence of the NC from the constricted tunnel into the exit port (Fig. 4A). The

detection of these resonances therefore demonstrates the potential to structurally dissect the behavior of NCs that are close to, and potentially even within, the exit vestibule.

Further from the PTC, from residues K58–M5, our simulations indicate that the mobility of each residue continues to increase (Fig. 4 C and D). We observed, however, that the intensities of NC resonances in this region were significantly less than those of residues closer to the PTC. In particular, clusters of resonances in the N-terminal region, encompassing M5–S9 and V37–V40, were broadened beyond detection as well as resonances around T92/G93, which showed a significant (~97%) attenuation in NMR signal (Fig. 1E), indicating the existence of interactions between the NC and the ribosome surface. Interestingly, the line broadening observed in the N-terminal region of the RNC was also observed for isolated αSyn in the presence of ribosomes (Fig. S2C), suggesting a similar mode of interaction, although substantially weaker in the absence of a covalent link to the ribosome (Fig. S4F). Such interactions have previously been observed for RNCs, by NMR for FLN5 (22, 25) and SH3 (24), by fluorescence methods for the IDP PIR (11), and by optical force spectroscopy for T4 lysozyme (9). In the latter two cases, interactions were driven at least partially by the high negative charge density of the ribosome surface, and modulations of the electrostatic environment by ionic strength (9) or differently charged variants of the NC (11) were shown to perturb the binding interaction. In the present study, the large number of resolved NC resonances provided us with the ability to unravel sequence determinants of these interactions, from the identification of αSyn residues interacting with the ribosome surface. We conclude that the net positive charge of the N-terminal region (resulting from the αSyn KTKEGV repeat motif) induces electrostatic interactions with the ribosome surface, which in isolation are reduced in the reverse-charged K6–60E αSyn variant, in which positive charges are eliminated, or increased in the more positively charged H_6-tagged αSyn (Fig. S4). We also observed that interactions of the clusters around M5–S9, V37–V40, and T92–G93 are associated with the aromatic residues F4, Y39, and F94 (Fig. 1E). As the interaction pattern does not appear to correlate with the known region of hydrophobicity within αSyn (Fig. 1E), this would indicate that there may be a specific affinity of the ribosome surface for aromatic residues. Interestingly, similar patterns of NMR line broadening have been observed for αSyn within bacterial (32) and mammalian cells (49), which suggests that there may be a common role for charged and aromatic residues in governing protein interactions both with the ribosome surface and with other components of the cellular milieu.

NMR intensity analysis provides a sensitive and high-resolution probe of ribosome surface interactions, but due to the interplay of ^1H and ^{15}N relaxation processes their quantitative interpretation in terms of NC dynamics is not currently possible. We therefore also measured ^1H linewidths for 31 NC residues from V48–A124, to provide a quantitative estimate of ribosome binding (Fig. 2 and Fig. S3 B–D). Relaxation rates for the bound state of the NC were evaluated using an ensemble model of the RNC in which the correlation time of the NC was set equal to that of the ribosome (Fig. S3C), and on this basis we determined an average bound state population of 0.45 ± 0.25% for residues in this segment of the NC (Fig. S3D). Although this interaction is rather weak, residues that were unobservable by NMR (M5–S9 and V37–V40) are likely to be interacting more strongly with the ribosome surface. Moreover, because the bound state may represent a set of interconverting states rather than a single rigid conformation, the collective effect of many weak interactions means that the total population of the NC in association with the surface at any given instant may be substantially greater than 0.45% (Fig. 2C).

Finally, we have reported residue-specific details of the interaction of the ribosome-associated chaperone TF with a NC. Intensity reductions of ~70% were observed for residues K21–G111 of the αSyn RNC in the presence of TF. Although this region spans the net positively charged N-terminal region (K21–E61), the hydrophobic NAC region (Q62–V95), and part of the negatively charged C-terminal region (K96–G111), the observed

broadening was found to be approximately uniform and hence independent of the previously identified preferences of TF for basic and hydrophobic substrates (19, 21). Instead, our structural modeling indicates that the observed broadening can be better correlated with those residues able to reach the TF cradle and its associated binding sites (21) (Fig. 4B). These NMR data indicate that 52 residues are necessary from the PTC to initiate an interaction with TF, with G111 being the first residue to be significantly perturbed in intensity. Cross-linking studies (50) as well as theoretical calculations based on the crystal structure of ribosome-bound TF (15) have found similar minimum lengths to be necessary for NC–TF contact formation (47 and 43 residues, respectively). The results described here add residue-specific detail to these previous findings, confirming that NC lengths of about 50 residues are required to initiate interactions with TF.

In summary, this study begins to describe the structural and dynamic characteristics of disordered NCs during biosynthesis by examining the behavior of αSyn, an IDP associated with PD and related neurodegenerative conditions. Because αSyn is free from competition with CTF processes encountered by globular proteins, this study provides an insight into the earliest events experienced by emerging NCs, before the onset of CTF. The results show that the disordered structural ensemble of αSyn is not strongly perturbed when tethered to the ribosome, although with the sensitivity of the NMR measurements it was possible to identify and characterize very weak interactions of the NC with ribosomal proteins near the exit tunnel. Such interactions, mediated by charge and aromatic residues, are also likely to be determining factors that affect CTF of globular proteins, particularly because the ribosome is associated with having a direct chaperoning capacity (8, 9). Furthermore, although αSyn is a weak TF substrate, we could show that TF interacts with the N-terminal ~110 αSyn residues, including the positively charged N-terminal region, the hydrophobic NAC region, as well as, unexpectedly, residues of the negatively charged C-terminal region. This study shows that even weak substrates, including residues not known to bind TF, are affected by the presence of the chaperone, indicating that an interplay exists between the surface of the ribosome and that of the TF cradle upon the immediate exit of a NC from the ribosome. These observations have implications for understanding the CTF process, because the folding of a NC may not only be assisted by interactions with the ribosome surface, but also by the extent of TF involvement, resulting in a complex folding landscape. Such interactions could thus have a protective role for emerging NCs, particularly those likely to possess substantial regions of disorder, by preventing cotranslational misfolding induced by nonnative intra- or intermolecular interactions during biosynthesis (51).

Materials and Methods

Detailed materials and methods are given in *SI Materials and Methods*.

Preparation of αSyn RNCs. The αSyn gene was cloned into a pLDC-17 vector (34) and site-directed mutagenesis was used to introduce a TEV protease cleavage sequence between the N-terminal H_6-tag and αSyn. Uniformly ^{15}N-labeled RNCs were expressed in *E. coli* and purified as described previously (34). TEV protease was used to cleave the H_6-tag from the RNCs following nickel affinity chromatography.

Preparation of TF. Isotopically labeled TF, including selective protonation of Ile, Leu, and Val methyl side chains, was produced in *E. coli* according to standard procedures.

Detection of RNCs. RNC samples collected during purification or NMR acquisition were run on Bis-Tris polyacrylamide gels (pH 5.8) before Western blot. Polyclonal rat anti-αSyn (epitope residue 15–123) (BD Laboratories) and polyclonal rabbit anti-SecM (epitope SecM motif) antibodies were used to detect the NC.

NMR Spectroscopy. NMR data were acquired at 4 °C on a 700-MHz Bruker Avance III spectrometer with TXI cryoprobe. The ^1H-^{15}N SOFAST-HMQC (35) spectra were recorded using nonuniform weighted sampling (36). ^{15}N-XSTE and ^1H stimulated echo (STE) diffusion experiments were acquired using a

diffusion delay of 100 ms and bipolar trapezoidal gradient pulses (total length, 4 ms; shape factor, 0.9) with strengths of 0.028 and 0.532 Tm^{-1}.

Coarse-Grained MD Simulations of the αSyn RNC. An atomic model of a stalled NC on the ribosome was derived from cryoEM data (43) by molecular-dynamics flexible fitting (52). To produce an αSyn RNC starting model, the original NC sequence in the model was replaced and extended to the sequence of the αSyn RNC using Swiss-PDB Viewer. TF bound to the ribosome was modeled based on the cryoEM data of the ribosome–TF complex (50) and the structure of TF (14, 15). Simulations of the αSyn RNC were performed in Gromacs (53) using a version of the tube model (42), known as the CamTube force field using a 2.4-μs trajectory. The NC mobility for each residue was calculated as the RMSF from the average position of the CA atoms within the trajectory and amide S^2 generalized order parameters were calculated from an ensemble of 8,000 all-atom structures.

1. Liang ST, Xu YC, Dennis P, Bremer H (2000) mRNA composition and control of bacterial gene expression. *J Bacteriol* 182(11):3037–3044.
2. Bhushan S, et al. (2010) α-Helical nascent polypeptide chains visualized within distinct regions of the ribosomal exit tunnel. *Nat Struct Mol Biol* 17(3):313–317.
3. Lu J, Deutsch C (2005) Secondary structure formation of a transmembrane segment in Kv channels. *Biochemistry* 44(23):8230–8243.
4. Ciryam P, Morimoto RI, Vendruscolo M, Dobson CM, O'Brien EP (2013) In vivo translation rates can substantially delay cotranslational folding of the Escherichia coli cytosolic proteome. *Proc Natl Acad Sci USA* 110(2):E132–E140.
5. Zhang G, Ignatova Z (2011) Folding at the birth of the nascent chain: Coordinating translation with co-translational folding. *Curr Opin Struct Biol* 21(1):25–31.
6. Dobson CM (2003) Protein folding and misfolding. *Nature* 426(6968):884–890.
7. Frydman J, Erdjument-Bromage H, Tempst P, Hartl FU (1999) Co-translational domain folding as the structural basis for the rapid de novo folding of firefly luciferase. *Nat Struct Biol* 6(7):697–705.
8. Hoffmann A, et al. (2012) Concerted action of the ribosome and the associated chaperone trigger factor confines nascent polypeptide folding. *Mol Cell* 48(1):63–74.
9. Kaiser CM, Goldman DH, Chodera JD, Tinoco I, Jr, Bustamante C (2011) The ribosome modulates nascent protein folding. *Science* 334(6063):1723–1727.
10. Ellis JP, Culviner PH, Cavagnero S (2009) Confined dynamics of a ribosome-bound nascent globin: Cone angle analysis of fluorescence depolarization decays in the presence of two local motions. *Protein Sci* 18(10):2003–2015.
11. Knight AM, et al. (2013) Electrostatic effect of the ribosomal surface on nascent polypeptide dynamics. *ACS Chem Biol* 8(6):1195–1204.
12. Gershenson A, Gierasch LM (2011) Protein folding in the cell: Challenges and progress. *Curr Opin Struct Biol* 21(1):32–41.
13. Preissler S, Deuerling E (2012) Ribosome-associated chaperones as key players in proteostasis. *Trends Biochem Sci* 37(7):274–283.
14. Kramer G, et al. (2002) L23 protein functions as a chaperone docking site on the ribosome. *Nature* 419(6903):171–174.
15. Ferbitz L, et al. (2004) Trigger factor in complex with the ribosome forms a molecular cradle for nascent proteins. *Nature* 431(7008):590–596.
16. Kaiser CM, et al. (2006) Real-time observation of trigger factor function on translating ribosomes. *Nature* 444(7118):455–460.
17. Mashaghi A, et al. (2013) Reshaping of the conformational search of a protein by the chaperone trigger factor. *Nature* 500(7460):98–101.
18. Patzelt H, et al. (2002) Three-state equilibrium of Escherichia coli trigger factor. *Biol Chem* 383(10):1611–1619.
19. Patzelt H, et al. (2001) Binding specificity of Escherichia coli trigger factor. *Proc Natl Acad Sci USA* 98(25):14244–14249.
20. Raine A, Lovmar M, Wikberg J, Ehrenberg M (2006) Trigger factor binding to ribosomes with nascent peptide chains of varying lengths and sequences. *J Biol Chem* 281(38):28033–28038.
21. Saio T, Guan X, Rossi P, Economou A, Kalodimos CG (2014) Structural basis for protein antiaggregation activity of the trigger factor chaperone. *Science* 344(6184):1250494.
22. Hsu S-TD, et al. (2007) Structure and dynamics of a ribosome-bound nascent chain by NMR spectroscopy. *Proc Natl Acad Sci USA* 104(42):16516–16521.
23. Rutkowska A, et al. (2009) Large-scale purification of ribosome-nascent chain complexes for biochemical and structural studies. *FEBS Lett* 583(14):2407–2413.
24. Eichmann C, Preissler S, Riek R, Deuerling E (2010) Cotranslational structure acquisition of nascent polypeptides monitored by NMR spectroscopy. *Proc Natl Acad Sci USA* 107(20):9111–9116.
25. Cabrita LD, et al. (2016) A structural ensemble of a ribosome-nascent chain complex during co-translational protein folding. *Nat Struct Mol Biol* 23(4):278–285.
26. Christodoulou J, et al. (2004) Heteronuclear NMR investigations of dynamic regions of intact Escherichia coli ribosomes. *Proc Natl Acad Sci USA* 101(30):10949–10954.
27. Elcock AH (2006) Molecular simulations of cotranslational protein folding: Fragment stabilities, folding cooperativity, and trapping in the ribosome. *PLOS Comput Biol* 2(7):e98.
28. O'Brien EP, Christodoulou J, Vendruscolo M, Dobson CM (2012) Trigger factor slows co-translational folding through kinetic trapping while sterically protecting the nascent chain from aberrant cytosolic interactions. *J Am Chem Soc* 134(26):10920–10932.
29. Ingólfsson HI, et al. (2014) The power of coarse graining in biomolecular simulations. *Wiley Interdiscip Rev Comput Mol Sci* 4(3):225–248.
30. Dedmon MM, Lindorff-Larsen K, Christodoulou J, Vendruscolo M, Dobson CM (2005) Mapping long-range interactions in α-synuclein using spin-label NMR and ensemble molecular dynamics simulations. *J Am Chem Soc* 127(2): 476–477.
31. Li C, et al. (2008) Differential dynamical effects of macromolecular crowding on an intrinsically disordered protein and a globular protein: Implications for in-cell NMR spectroscopy. *J Am Chem Soc* 130(20):6310–6311.
32. Waudby CA, et al. (2013) In-cell NMR characterization of the secondary structure populations of a disordered conformation of α-synuclein within E. coli cells. *PLoS One* 8(8):e72286.
33. Nakatogawa H, Ito K (2001) Secretion monitor, SecM, undergoes self-translation arrest in the cytosol. *Mol Cell* 7(1):185–192.
34. Cabrita LD, Hsu ST, Launay H, Dobson CM, Christodoulou J (2009) Probing ribosome-nascent chain complexes produced *in vivo* by NMR spectroscopy. *Proc Natl Acad Sci USA* 106(52):22239–22244.
35. Schanda P, Brutscher B (2005) Very fast two-dimensional NMR spectroscopy for real-time investigation of dynamic events in proteins on the time scale of seconds. *J Am Chem Soc* 127(22):8014–8015.
36. Waudby CA, Christodoulou J (2012) An analysis of NMR sensitivity enhancements obtained using non-uniform weighted sampling, and the application to protein NMR. *J Magn Reson* 219:46–52.
37. Kirchdoerfer RN, Huang JJ-T, Isola MK, Cavagnero S (2007) Fluorescence-based analysis of aminoacyl- and peptidyl-tRNA by low-pH sodium dodecyl sulfate-polyacrylamide gel electrophoresis. *Anal Biochem* 364(1):92–94.
38. Ferrage F, Zoonens M, Warschawski DE, Popot JL, Bodenhausen G (2003) Slow diffusion of macromolecular assemblies by a new pulsed field gradient NMR method. *J Am Chem Soc* 125(9):2541–2545.
39. Amand B, Pochon F, Lavalette D (1977) Rotational diffusion of *Escherichia coli* ribosomes. I. - Free 70 S, 50 S and 30 S particles. *Biochimie* 59(10):779–784.
40. Tomic S, Johnson AE, Hartl FU, Etchells SA (2006) Exploring the capacity of trigger factor to function as a shield for ribosome bound polypeptide chains. *FEBS Lett* 580(1):72–76.
41. Lakshmipathy SK, Gupta R, Pinkert S, Etchells SA, Hartl FU (2010) Versatility of trigger factor interactions with ribosome-nascent chain complexes. *J Biol Chem* 285(36):27911–27923.
42. Banavar JR, Maritan A (2007) Physics of proteins. *Annu Rev Biophys Biomol Struct* 36: 261–280.
43. Bhushan S, et al. (2011) SecM-stalled ribosomes adopt an altered geometry at the peptidyl transferase center. *PLoS Biol* 9(1):e1000581.
44. Sandikci A, et al. (2013) Dynamic enzyme docking to the ribosome coordinates N-terminal processing with polypeptide folding. *Nat Struct Mol Biol* 20(7):843–850.
45. Papoian GA (2008) Proteins with weakly funneled energy landscapes challenge the classical structure-function paradigm. *Proc Natl Acad Sci USA* 105(38):14237–14238.
46. Camilloni C, Vendruscolo M (2013) A relationship between the aggregation rates of α-synuclein variants and the β-sheet populations in their monomeric forms. *J Phys Chem B* 117(37):10737–10741.
47. Bah A, et al. (2015) Folding of an intrinsically disordered protein by phosphorylation as a regulatory switch. *Nature* 519(7541):106–109.
48. Deleersnijder A, Gerard M, Debyser Z, Baekelandt V (2013) The remarkable conformational plasticity of alpha-synuclein: Blessing or curse? *Trends Mol Med* 19(6):368–377.
49. Theillet FX, et al. (2016) Structural disorder of monomeric α-synuclein persists in mammalian cells. *Nature* 530(7588):45–50.
50. Merz F, et al. (2008) Molecular mechanism and structure of Trigger Factor bound to the translating ribosome. *EMBO J* 27(11):1622–1632.
51. Brandt F, et al. (2009) The native 3D organization of bacterial polysomes. *Cell* 136(2):261–271.
52. Gumbart J, Schreiner E, Wilson DN, Beckmann R, Schulten K (2012) Mechanisms of SecM-mediated stalling in the ribosome. *Biophys J* 103(2):331–341.
53. Pronk S, et al. (2013) GROMACS 4.5: a high-throughput and highly parallel open source molecular simulation toolkit. *Bioinformatics* 29(7):845–854.
54. Sivashanmugam A, et al. (2009) Practical protocols for production of very high yields of recombinant proteins using *Escherichia coli*. *Protein Sci* 18(5):936–948.
55. Best RB, de Sancho D, Mittal J (2012) Residue-specific α-helix propensities from molecular simulation. *Biophys J* 102(6):1462–1467.
56. Betancourt MR, Thirumalai D (1999) Pair potentials for protein folding: Choice of reference states and sensitivity of predicted native states to variations in the interaction schemes. *Protein Sci* 8(2):361–369.
57. Ernst RR, Bodenhausen G, Wokaun A (1987) *Principles of Nuclear Magnetic Resonance in One and Two Dimensions* (Oxford Univ Press, New York).
58. Johnson E, Showalter SA, Brüschweiler R (2008) A multifaceted approach to the interpretation of NMR order parameters: A case study of a dynamic α-helix. *J Phys Chem B* 112(19):6203–6210.
59. Koppel DE (1974) Study of *Escherichia coli* ribosomes by intensity fluctuation spectroscopy of scattered laser light. *Biochemistry* 13(13):2712–2719.

BIOPHYSICS AND COMPUTATIONAL BIOLOGY

Supporting Information

Deckert et al. 10.1073/pnas.1519124113

SI Materials and Methods

Preparation of αSyn RNCs and 70S Ribosomes from *E. coli*. Uniformly ^{15}N-labeled RNCs were overexpressed in *E. coli* using enhanced minimal media (EM9), adapted from Sivashanmugam et al. (54) and purified as described previously (34). During purification, the RNCs were isolated using Ni^{2+} affinity chromatography and TEV protease was used to remove the H$_6$-tag, before sucrose density ultracentrifugation. The purified RNC samples were concentrated and buffer exchanged into Tico buffer (10 mM Hepes, 30 mM NH$_4$Cl, 12 mM MgCl$_2$, 5 mM EDTA, and 2 mM BME, pH 7.0) to 300 μL for NMR spectroscopy. The ^{15}N-labeled 70S ribosomes were prepared in a similar manner to the RNC samples with the omission of both the affinity chromatography and TEV protease cleavage steps. Unlabeled 70S ribosomes were prepared from *E. coli* cultures grown in LB medium. The concentration of 70S ribosomes was calculated using 1 Abs$_{260}$ = 24 pmol.

Detection and Integrity of RNCs. RNC samples are collected during purification or NMR acquisition at regular intervals and run on Bis-Tris polyacrylamide gels (pH 5.8) before immunodetection by Western blot, using enhanced chemiluminescence. The low pH conditions of the polyacrylamide gels retain the ester bond between the last incorporated amino acid and the tRNA (37), such that the tRNA-bound RNCs migrate with an additional ∼25 kDa (mass tRNA). The released αSyn NC has a calculated molecular weight of ∼18 kDa (ExPASy ProtParam) but migrates with an apparent molecular weight of ∼20 kDa. Western blot (Fig. S1 *D* and *F*) and ^{15}N diffusion (Fig. S1 *G–I*) were used in tandem to determine the lifetime of the sample, to ensure NMR analysis reflected only intact RNC species. NC occupancy was determined by Western blot analysis using isolated αSyn as a standard for protein concentration. The ^{15}N-edited and ^{15}N-filtered ^{1}H 1D experiments were used to determine the extent of ribosomal background, which was calculated to be less than 5% across all samples.

Preparation of TF. TF was expressed in deuterated EM9 media supplemented with metabolic precursors, which were selectively protonated at methyl groups for isoleucine (2-ketobutyric acid-4-^{13}C, 3-d$_2$ (Sigma-Aldrich), leucine, and valine (2-keto-3(methyl-d$_3$)-butyric acid-4-^{13}C, 3-d$_1$ (Sigma-Aldrich) for selective methyl labeling. Following lysis, TF was purified using Ni-nitrilotriacetic acid (NTA) chromatography, followed by H$_6$-tag removal using TEV protease and size-exclusion chromatography. Pure TF was concentrated and buffer exchanged into Tico buffer.

NMR Spectroscopy. NMR data were acquired for the αSyn RNC at 16.4 T (700 MHz) at 277 K using a Bruker Avance III spectrometer (Bruker BioSpin) equipped with a TXI cryoprobe. The ^{1}H-^{15}N SOFAST-HMQC (35) spectra of the αSyn RNC were recorded using nonuniform weighted sampling methods (36) with 1,024 complex points and a sweep width of 10,504 Hz in the direct (^{1}H) dimension and 122 complex points and a sweep width of 1,845 Hz in the indirect (^{15}N) dimension with a recycle time of 50 ms. The ^{15}N-edited XSTE diffusion measurements (38) were recorded by using a diffusion delay of 100 ms, and bipolar trapezoidal gradient encoding pulses of a total length of 4 ms and strengths corresponding to 5% (0.028 Tm^{-1}) and 95% (0.532 Tm^{-1}) of the maximum gradient strength (0.56 Tm^{-1}). The SOFAST-HMQC and XSTE measurements were carried out in an interleaved manner, allowing the integrity of the RNC to be continuously ascertained. NMR data were processed and analyzed by NMRPipe and Sparky software packages.

The ^{1}H Linewidth Analysis. ^{1}H cross-sections of ^{1}H-^{15}N SOFAST-HMQC spectra of isolated αSyn and the αSyn RNC spectra were processed with 12 Hz exponential apodization and fitted to a sum of Lorentzian functions to determine ^{1}H R_2 rates.

TF Titration and Analysis. The ^{15}N- and ^{13}C-edited 1D envelopes were recorded for the RNC, before the addition of TF to the samples. The different labeling schemes permitted the monitoring of the ^{15}N-labeled αSyn NC as well as the ^{2}H-TF that was selectively ^{13}C-labeled and protonated at all Ile, Leu, and Val side chain methyl groups. The ribosome concentration (Ab$_{260}$) measured for the RNC was 6.5 μM with a NC occupancy of 62% (i.e. NC concentration was 4.0 ± 0.4 μM). TF was added according to the ribosome concentration starting with 0.2 up to 0.4, 0.6, 0.8, 1, 1.5, 2, and 3 molar equivalents. Experiments were repeated in a similar manner (with 0.25, 0.5, 0.75, 1, 1.5, 2 and 5 molar equivalents of TF) for the interaction of TF with unoccupied 70S ribosomes at 5 μM concentration. For analysis, the integrals of the amide (or methyl) envelope were determined and normalized relative to a sample of isolated TF (10 μM). These were subsequently scaled according to the ribosome concentration for comparative analysis with RNCs. In these measurements, the contributions arising from the TF monomer/dimer equilibrium were considered to be minimal and thus were not included in the analysis.

Modeling of the *E. coli* 70S Stalled with an αSyn NC. An atomic model of a stalled NC on the ribosome was derived from cryoEM data (43) by molecular-dynamics flexible fitting (52). The original NC sequence in the model was replaced and extended to the sequence of the αSyn RNC using Swiss-PDB Viewer. TF bound to the ribosome was modeled based on the cryoEM data of the ribosome–TF complex (50) and the atomic structure of TF (14, 15). The NC mobility for each residue was calculated as the RMSF from the average position of CA atoms within the trajectory.

Coarse-Grained MD Simulations of the αSyn RNC in the Presence and Absence of TF. Coarse-grained simulations of the αSyn RNC were performed using a version of the tube model (42), known as the CamTube force field, which was implemented in Gromacs (53) via tabulated potentials. Each amino acid is represented by its five backbone atoms (N, H, CA, C, and O) and one atom (CB) has been used to model side-chains with the length of the CA–CB bond being amino acid-dependent. The bonded interactions are taken from the Amber force field (55). The tube-like behavior is obtained by imposing a hard sphere potential on all of the atoms. In addition, hydrogen bonding is modeled as Lennard-Jones interactions between pairs of O and H atoms, whereas hydrophobic and electrostatic interactions are introduced by residue-specific contact potentials implemented only between CB atoms of the residue pairs using the square well function. These potentials are adapted from lattice models of protein folding and parameterized based on the contact frequencies between amino acid pairs in the PDB (56). Additionally, a curvature penalty was introduced into the CamTube force field in form of a weak repulsive force between C and H atoms that are separated by two or three residues along the protein chain. Amber force field parameters were changed for CB-CA-N-C and CB-CA-C-N dihedral angles to reproduce correct Ramachandran plots in the CamTube force field. Within the CamTube model, the ribosome and TF are represented as frozen hard spheres with a 5-Å radius centered on P and CA carbon atoms for RNA and protein molecules, respectively. The system was simulated using a stochastic dynamics algorithm with a time step of 2 fs together with the LINCS algorithm

to constrain bond lengths. To enhance the NC sampling of the available space all simulations were performed at 345 K and run for 2.4 μs. For analysis we calculated the minimum distance between the CA atoms of the NC and the CA and P atoms of the ribosomal surface within six distance ranges (<6, 10, 15, 20, 25, and >25) for which the ribosome surface was colored accordingly.

Analysis of the MD Trajectory. Estimates of ^{1}H R_2 relaxation rates for a rigid bound state were calculated, as an ensemble average of 50 all-atom RNC structures, from the sum of ^{1}H-^{1}H dipolar interactions (57):

$$R_{2,i} = \left\langle \sum_{j \in H \text{ atoms}} \frac{1}{5} \left(\frac{\mu_0}{4\pi}\right)^2 \frac{\hbar^2 \gamma_H^4 S_{ij}^2 \tau_c}{r_{ij}^6} \right\rangle, \quad \text{[S1]}$$

where γ_H is the proton gyromagnetic ratio, $S_{ij}^2 = 1$ are the generalized order parameters for internuclear bond vectors, and $\tau_c = 3.9$ μs is the ribosome rotational correlation time at 277 K in H_2O (39). Only the zero frequency spectral density has been considered, because given the slow tumbling of the ribosome the contribution from higher frequency terms is negligible.

Amide S^2 generalized order parameters were calculated from an ensemble of 8,000 all-atom RNC structures, where θ and ϕ are angles of the N–H bond vector relative to the fixed molecular reference frame (58):

$$S^2 = \frac{4\pi}{5} \sum_{m=-2}^{2} \langle Y_{2m}(\theta, \phi) \rangle \langle Y_{2m}^*(\theta, \phi) \rangle. \quad \text{[S2]}$$
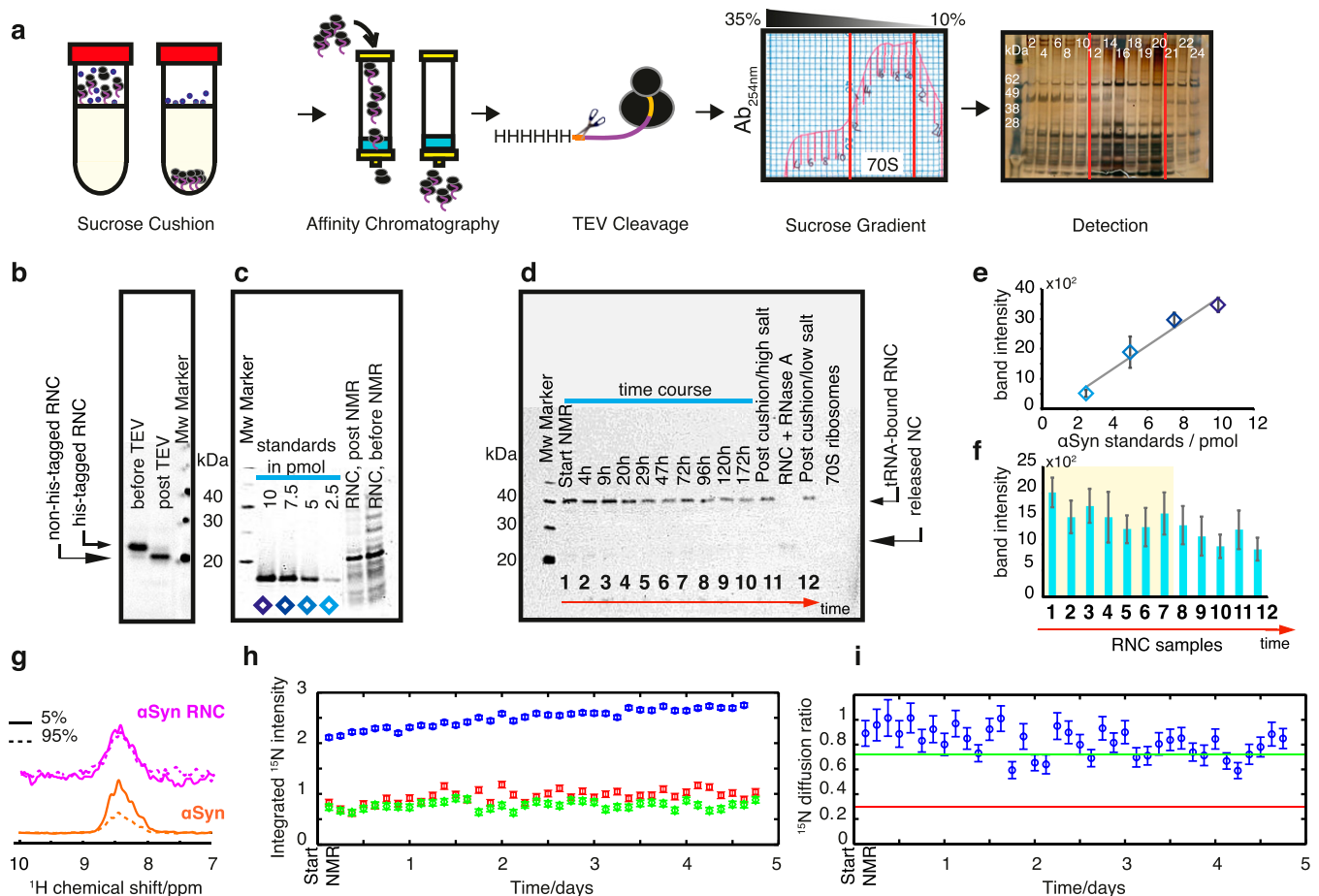
Fig. S1. RNC purification and monitoring of sample stability of ^{15}N-labeled αSyn RNCs. (A) αSyn RNC purification involves a four-stage strategy including a sucrose cushion to pellet ribosomal material, nickel affinity chromatography to selectively enrich NC occupied ribosomes using the N-terminal H_6-tag, purification tag removal using a TEV protease, and a sucrose gradient ultracentrifugation step. The 70S-containing fractions (indicated by red borders) were identified using absorbance measurements at 254 nm and silver staining of SDS/PAGE. (B) Anti-SecM Western blot of samples (10 pmol) collected during RNC purification. A band shift of ∼0.6 kDa is observed in the NC following TEV cleavage to remove H_6-tag (lane 1 to lane 2). (C) Ribosome occupancy determination: anti-αSyn Western blot RNC sample (10 pmol, 70S ribosome concentration) relative to αSyn protein standards. (D) Anti-SecM Western blot of the RNC sample during its NMR acquisition period. The band at ∼40 kDa is indicative of a tRNA-bound RNC species (37). (E) NC occupancy as determined by Western blot: band intensities of isolated αSyn standards (from C) plotted against concentrations, alongside the corresponding calibration used for quantitative analysis. (F) NC integrity as assessed over time. Band intensities of RNC samples loaded in D are plotted over time to monitor the integrity of the NC species over the course of NMR data acquisition. The timeframe during which the sample is deemed to be intact is highlighted in yellow. (G) The ^{15}N-XSTE diffusion NMR measurements, at 5% and 95% gradient strengths as indicated, for an attached αSyn NC and isolated αSyn. (H) The integrated intensities of the ^{15}N-edited 1D envelope over time (blue circles) and ^{15}N-stimulated echo diffusion measurements (38) on the αSyn RNC at 5% (red squares) and 95% (green squares) of the maximum gradient strength. Error bars indicate the SEM derived from measurements of spectral noise. (I) Intensity ratio I$_{95\%}$/I$_{5\%}$ of the αSyn RNC during NMR data acquisition (average I$_{95\%}$/I$_{5\%}$ ∼0.82 ± 0.12 and D = 7.67 ± 5.56 × 10^{-12} m^2·s^{-1}). The green line represents the intensity ratio measured for intact 70S ribosomes [hydrodynamic radius r_h = 12.6 nm (59), diffusion coefficient D = 1.1 × 10^{-11} m^2·s^{-1} at 277 K in H_2O]. The red line indicates the intensity ratio of isolated αSyn [r_h = 2.72 nm (30), D = 5 × 10^{-11} m^2·s^{-1} at 277K in H_2O].

Fig. S2. NMR experiments of 70S ribosomes and isolated αSyn. NMR experiments of isolated αSyn in the presence of 70S ribosome, recorded under the same conditions as the αSyn RNC sample (277 K in Tico buffer at pH 7.0). (*A*) Overlay of ^{1}H-^{15}N SOFAST-HMQC spectrum of the αSyn RNC in magenta with the ^{1}H-^{15}N SOFAST-HMQC spectrum of ^{15}N-labeled 70S ribosomes (dark gray). The ribosome spectrum was recorded to identify potential ribosomal peaks in the αSyn RNC spectrum originating from background labeling of the ribosomal protein L7/L12 (27) (dark gray). (*B*) The ^{1}H-^{15}N SOFAST HMQC spectrum of isolated αSyn with backbone assignment. Boxed area in *B* expanded for clarification. (*C*) Relative cross-peak intensities of WT αSyn (orange) in the presence and absence of 1 mol eq 70S ribosomes.

Fig. S3. Chemical shift changes and lineshape analysis for the αSyn RNC and isolated αSyn. (*A*) $\Delta\delta_{NH}$ chemical shift changes between the isolated αSyn protein and the αSyn RNC ($\Delta\delta_{NH} = [\Delta\delta_H^2 + (\Delta\delta_N/5)^2]^{1/2}$/ppm). (*B*) Transverse relaxation rate (R_2) determined for αSyn bound to the ribosome (magenta) and αSyn in isolation (orange). R_2 values were resolved by fitting the NMR resonances to Lorentzian lineshapes. Because $^3J_{HNHA}$ couplings were not resolved, we note that these relaxation rates are expected to contain an additional contribution of *ca.* 20–30 s^{-1} (6–10 Hz). (*C*) The ^{1}H amide linewidths estimated for a rigid ribosome-associated state by averaging of ^{1}H-^{1}H dipolar interactions across an ensemble of all-atom models of the αSyn RNC. Calculations were repeated to both include (magenta) and exclude (orange) the effect of ribosomal protons. (*D*) Estimation of ribosome-bound populations of the αSyn RNC using measured linewidths of free the αSyn (Fig. 2*B*) and calculated bound-state linewidths (Fig. S3*C*), $R_{2,obs} = R_{2,free} + p_{bound}S^2R_{2,rigid}$ (black dashed line). The red line and shaded area show the mean ± SD of linewidths measured for the αSyn RNC (residues 48–124) and the associated bound-state population.

Fig. S4. NMR spectra and relative cross-peak intensities of the αSyn charge variants. (A) Charge variants constructed to investigate the effect of electrostatics. Of the 15 Lys residues within the αSyn sequence, the first 11 (residues K6 to K60) were mutated to Glu, lowering the pI from 4.67 (WT) to 3.63 (K6–60E). Having an N-terminal hexa-histidine (H₆) tag increased the pI to 5.22. (B) The ^{1}H-^{15}N HSQC spectrum of H₆-αSyn (green) and in (C) overlaid with WT αSyn (orange). (D) The ^{1}H-^{15}N SOFAST-HMQC spectrum of K6–60E αSyn (blue) and in (E) overlaid with WT αSyn (orange). (F) Relative cross-peak intensities of K6–60E αSyn (blue), WT αSyn (orange, as in Fig. S2C), and H₆-αSyn (green) in the presence and absence of 1 mol eq 70S ribosomes. Cross-peak intensities of the αSyn RNC relative to isolated αSyn in the presence of ribosomes (pink, as in Fig. 1E) have been plotted again for better comparison between the line broadenings observed in the N-terminal region of the RNC as well as isolated αSyn.

Fig. S5. Chemical shift and peak intensity perturbations of isolated αSyn and the αSyn RNC upon addition of TF. (*A*) Δδ$_{NH}$ chemical shift changes between the αSyn RNC in the presence and absence of TF and (*B*) between isolated αSyn in the presence and absence of TF (Δδ$_{NH}$ = [Δδ$_H^2$ + (Δδ$_N$/5)^2]$^{1/2}$/ppm). (*C*) Relative cross-peak intensities between isolated αSyn in the presence of both 70S ribosomes and TF compared with αSyn+70S only (gray circles), between αSyn+TF compared with isolated αSyn at 5 μM (green circles), and 100 μM (orange circles) equivalent concentrations. (*D*) The ^{13}C-edited 1D envelopes of 10 μM TF (green), in the presence of the αSyn RNC (blue) and the presence of 70S ribosomes (gray).

Movie S1. αSyn NCs emerging from the ribosome.

Movie S2. αSyn NCs emerging from the ribosome in the presence of TF.